36c.0 COMBINING IN-SITU AND EX-SITU CHARACTERIZATION TO UNDERSTAND CRYSTALLOGRPHIC TEXTURE DEVELOPMENT IN METAL ADDITIVE MANUFACTURING

Jonah Klemm-Toole (Mines)
Faculty: Amy Clarke (Mines)
Industrial Mentor: TBD

This project was initiated in Spring 2019 and is supported by an Office of Naval Research (ONR) Multidisciplinary University Research Initiative (MURI). The research performed during this project will serve as the contribution of Jonah Klemm-Toole as a Post-Doctoral Fellow in CANFSA.

36c.1 Project Overview and Industrial Relevance

The emergence of metal additive manufacturing (MAM) has unlocked the possibility to create complex geometries with location and orientation specific properties. The vast parameter space available in MAM enables the creation of unique microstructures that are not possible with conventional processing. However, as MAM is not a fully mature technology, there is not a full understanding of processing-microstructure-property relationships. Recent reviews by the National Academy of Sciences (NAS) [36.1], the Federal Aviation Administration (FAA) [36.2], and National Institute for Standards and Technology [36.2] have identified anisotropic mechanical properties as a characteristic of MAM that limits the broad implementation of this transformative technology. **Figure 36.1** illustrates the expected application of MAM over time as the technology matures [36.3]. In order to apply MAM to high value, failure critical components such as gas turbine airfoils, the origins of anisotropic mechanical properties in MAM must be investigated further. Crystallographic texture, or non-random orientations of grains, is expected to be a major contributor to anisotropic mechanical properties observed in MAM. In this project we aim to combine in-situ characterization, e.g. radiography during laser melting to simulate laser-based MAM, with ex-situ characterization such as scanning electron microscopy (SEM) and electron backscatter diffraction (EBSD) in order obtain a deeper understanding of crystallographic texture development in MAM. It is expected that the outcome of this project will contribute to a deeper understanding of processing-microstructure relationships and enable the broader implementation of MAM.

36c.2 Previous Work – Literature Review

The majority of literature related to crystallographic texture in MAM focuses on the observance and/or control of a ⟨100⟩ fiber texture, where a large fraction of the grains (more than random) are oriented such that a ⟨100⟩ direction is parallel to the build direction [36.4-36.5]. Although one ⟨100⟩ direction of a given grain may be parallel to the build direction, the other axes of the grain are generally random with respect to the MAM build. Dendrites in cubic metals typically to grow along ⟨100⟩ directions [36.6], and the columnar dendritic solidification often observed in MAM results in a high number of grains having a ⟨100⟩ direction parallel to the build direction. The ⟨100⟩ fiber texture can be suppressed if the equiaxed transition (CET) is induced. The CET refers to nucleation of different grain orientations in the supersaturated liquid ahead of a columnar solidifying front [36.7]. In essence, the majority of MAM literature focuses on controlling the CET in order to maintain (avoid the CET) or suppress (induce the CET) a ⟨100⟩ fiber texture. Very little work in the literature evaluates textures other than a ⟨100⟩ fiber texture.

Significant research has been conducted to better understand the CET to enable weld repair of single crystal gas turbine blades. **Figure 36.2** summarizes the key solidification conditions that result in the CET during laser welding of a single crystal alloy CMSX-4. **Figure 36.2(b)** shows an EBSD misorientation map which shows the substrate ⟨100⟩ orientation through the majority of the weld microstructure. A plot of thermal gradient (G) versus solidification velocity (V) in **Figure 36.2(c)** indicates that the majority of the weld is expected to be "columnar" which implies the weld should be the same orientation as the substrate. **Figure 36.2(b)** shows a weld that exhibits new grain orientations, corresponding to the G-V plot in **Figure 36.2(c),** which predicts that the CET would be induced in the weld. It is noteworthy that G decreases and V increases from the beginning to the end of solidification which implies that the top of the pool is the most likely location to have crossed the CET and show new grain orientations [36.8]. The variations in G and V from the beginning to end of solidification in the welds were predicted from simple heat transfer models that only consider conduction and do not account for latent heat of transformation. Furthermore, the CET model considers equilibrium solution partitioning and only diffusion mass transfer in the

liquid (no convention) to calculate constitutuional supercooling. Despite the simplicity of the models, they are able to reasonably predict the CET observed experimentally. Furthermore, **Figure 36.2** illustrates the utility of using single crystals to study the CET.

36c.3   Recent Progress

31.3.1   Experimental Design

The AM simulator at the Advanced Photon Source (APS) in Argonne National Laboratory was used to obtain in-situ radiography during laser melting and subsequent solidification to simulate laser based MAM. The objectives of the initial set of experiments at APS were to investigate 1) the influences of spot and raster melting strategies, 2) effects of laser power, 3) effects of single crystal substrate orientation, and 4) effects of composition on crystallographic texture and the occurrence of the CET during simulated MAM. **Figure 36.3** shows a schematic of the AM simulator in Sector 32 of the APS [36.9]. Specimens for the AM simulator were designed to have specific crystallographic orientations parallel to the laser beam shown in **Figure 36.3**, which is herein after referred to as the build direction. **Table 36.1** summarizes the specimens evaluated at the APS thus far, and only results from spot melts will be described here. Two alloys were evaluated which vary principally on molybdenum (Mo) content. R4 has a considerably higher Mo content than R2. R4 samples with a ⟨100⟩ and a ⟨110⟩ direction parallel to the build direction, and R2 samples with a ⟨110⟩ and ⟨111⟩ direction parallel to the build direction were investigated. Laser powers of 106, 156, 208, and 260 W for 1 ms in spot melting mode were also investigated.

31.3.2   In-Situ Radiography

Radiography obtained during laser melting and solidification was analyzed to measure the velocity of the solid liquid interface. **Figure 36.4(a)** shows an example radiograph of R2-111 during solidification. The white arrows point to the location of the solid-liquid interface at the beginning of solidification, and the red arrows point to the location of the interface at a later time. Radiography images were processed by dividing all images by the first image using ImageJ in order to minimize artifacts and highlight the solid-liquid interface. By tracking the progression of the solid liquid interface and accounting for the time between images, the solidification velocity was measured. **Figure 36.4(b)** shows a plot of solidification velocity (velocity of solid liquid interface) as a function of position from the bottom to the top of the melt pool for R2-111 samples melted with 104 W and 260 W for 1 ms. As predicted by heat transfer models in **Figure 36.2**, velocity is observed to increase from the bottom to the top of the melt pool. Furthermore, the lower laser power condition, 106 W for 1 ms, is observed to have a higher maximum solidification velocity. Based on the CET model shown graphically in **Figure 36.2**, higher solidification velocities are more likely to induce the CET, so it is expected that more new grains nucleated in the lower laser power conditions.

31.3.3   Ex-Situ SEM and EBSD

A representative set of superimposed EBSD inverse pole figure (IPF) and image quality (IQ) maps for R2-111 melted with the full range of laser powers investigated is shown in **Figure 36.5**. The coloring of the IPF maps corresponds to the crystallographic orientation parallel to the build direction. With decreasing laser power, more new grain orientations are observed in the EBSD maps. Higher solidification velocities and the resulting greater tendency to induce the CET are likely the cause of more new grains at the surface of the welds with lower laser power. Similar trends of lower laser powers resulting in new grain orientations at the top of the weld pools is observed in all samples investigated. Despite the observation of new grains at the surface of the pools at lower laser powers, the majority of the microstructure of the laser welds for all conditions exhibits the crystallographic orientation of the substrate.

The influence of substrate orientation on solidification microstructure of R4 melted with 106 W for 1 ms is shown in **Figure 36.6**. Both R4-100 **(a)** and R4-110 **(b)** show new grain orientations at the top of the weld as would be expected from the higher solidification velocity. The difference between the two samples lies in the orientation of the dendritic or cellular growth as indicated on the EBSD maps. **Figures 36.6 (c)** and **(d)** show ⟨100⟩ pole figures with the traces of the growth orientations indicated for R4-100 and R4-110, respectively. The traces of the growth orientations in both samples contain ⟨100⟩ directions suggesting that the growth is parallel to ⟨100⟩ directions and is likely dendritic rather than cellular. The distinction between cellular growth and dendritic growth is that dendrites grow along ⟨100⟩ directions and cells grow along any orientation parallel to the primary heat flow direction [36.6]. Similar trace analysis

cannot rule out dendritic growth in all samples evaluated.

The influence of composition on solidification microstructure is illustrated in **Figure 36.7** by showing SEM backscattered electron (BSE) micrographs of the top of welds made on R2-110 and R4-110 at 106 W for 1 ms. The (possible) dendrites observed at the top of the weld in R2-110 do not show secondary arms, whereas secondary arms are observed on the dendrites in the surface of the weld on R4-110. It is likely that the higher Mo content in R4 leads to more solute portioning and higher degrees of constitutional supercooling during solidification.

36c.4   Plans for Next Reporting Period

Ex-situ EBSD and SEM has been performed on the lowest and highest laser power spot melt conditions for all specimens. Analysis of in-situ radiography has only been performed on selection conditions. Work to follow in the next reporting period includes:

- EBSD of all laser power spot melt conditions

- Evaluation of solidification velocity parallel to dendrite growth directions by combining data from ex-situ EBSD and in-situ radiography

- EBSD and SEM of raster melts conditions

- Preparation of a journal article documenting the results from the first set of experiments at the APS

36c.5   References

[36.1]   D. Snyder, Computational and analytical methods in additive manufacturing, in: M. Schwalbe, (Ed.), Snyder Predictive theoretical and computational approaches for additive manufacturing: proceedings of a workshop, The National Academies Press, 2015, pp. 47-50.

[36.2]   M. Seifi, M. Gorelik, J. Walker, N. Hrabe, N. Shamsaei, S. Daniewicz, J.J. Lewandowski, "Progress towards metal additive manufacturing standardization to support qualification and standardization, JOM. 69:3 (2017) 439-455.

[36.3]   M. Gorelik, Additive manufacturing in the context of structural integrity, International Journal of Fatigue. 94 (2017) 168-177.

[36.4]   H.L. Wei, J. Mazumder, T. Debroy, Evolution of solidification texture during additive manufacturing, Scientific Reports. 5:16446 (2015) 1-7.

[36.5]   R.R. Dehoff, M.M. Kirka, W.J. Sames, H. Bilheux, A.S. Tremsin, L.E. Lowe, S.S. Babu, Site specific control of crystallographic grain orientation through electron beam additive manufacturing, Materials Science and Technology. 31:8 (2015) 931-938.

[36.6]   W. Kurz and D.J. Fisher, Solidification Microstructure, in: Fundamentals of Solidification, Fourth ed., Trans Tech Publications LTD, 1998, p. 68.

[36.7]   W. Kurz, C. Bezencon, M. Gaumann, Columnar to equiaxed transition in solidification processing, Science and Technology of Advnaced Materials. 2 (2001) 185-191

[36.8]   M. Gaumann, C. Bezencon, P. Canalis, W. Kurz, Single-crystal laser deposition of superalloys: processing-microstructure maps, Acta Materialia. 49 (2001) 1051-1062.

[36.9]   C. Zhao, K. Fezzaa, R.W. Cunningham, H. Wen, F. De Carlo, L. Chen, A.D. Rollett, T. Sun, Real-time monitoring of laser powder bed fusion process using high-speed X-ray imaging and diffraction, Scientific Reports. 7:3602 (2017) 1-11.
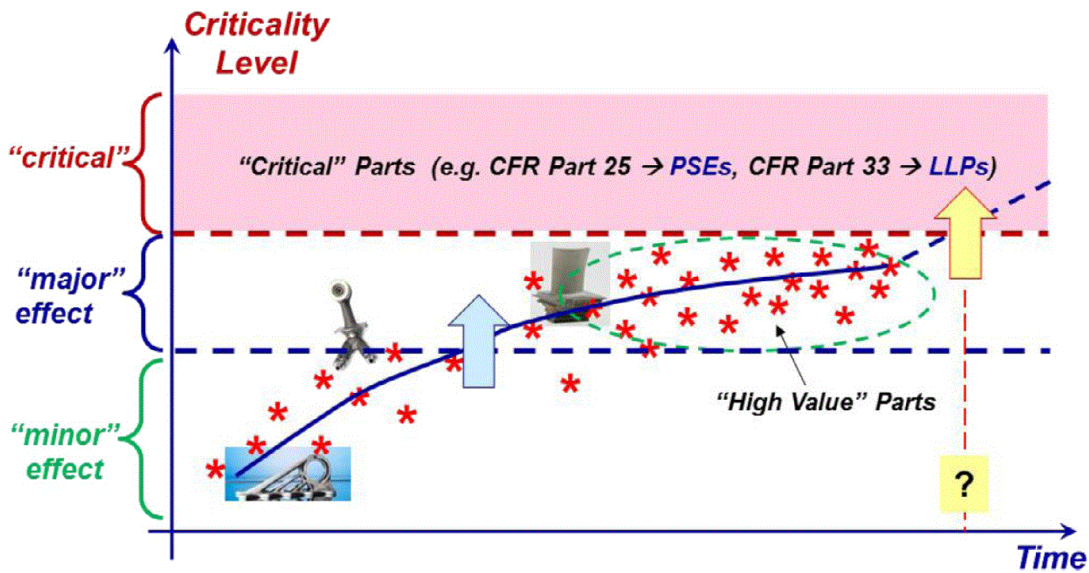
36c.6   Figures and Tables

Figure 36.1: Projected maturity of AM technology. With a better understanding of processing-microstructure-mechanical property relationships developed over time, AM can be applied to high value, failure critical components such as gas turbine airfoil components [36.3].
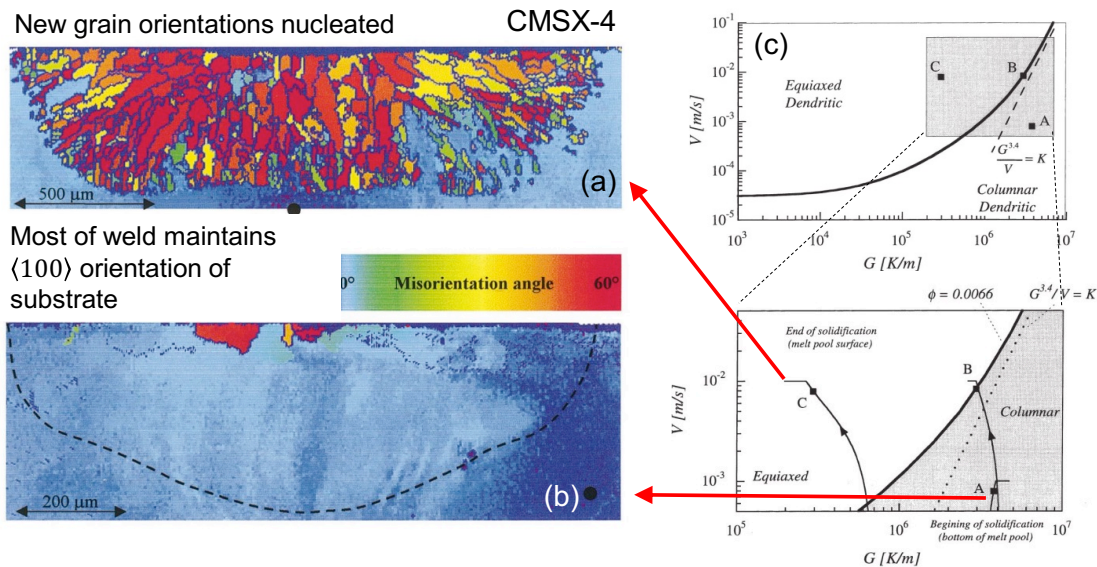

Figure 36.2: Influence of thermal gradient (G) and solidification velocity (V) on the columnar to equiaxed transition (CET) in laser melted single crystal Ni-based superalloy CMSX-4. (a) EBSD misorientation and image quality (IQ) map of a weld where the majority of melt pool has different crystallographic orientations due to the CET. (b) Same as (a) except the majority of the weld shows the same $\langle 100 \rangle$ orientation as the substrate. (c) Plots of G and V with a curve indicating the CET. The values of G and V for the laser melting parameters in (a) and (b) were calculated using heat transfer models. Heat transfer models predict that V increases from the bottom to the top of the melt pool. Plots adapted from [36.8].
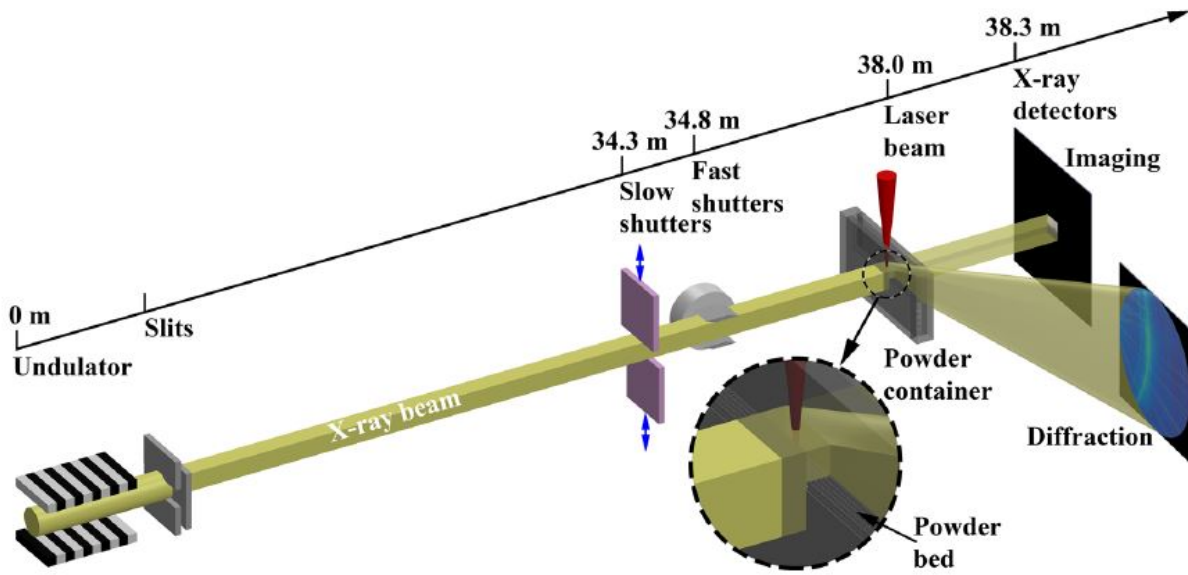
36.4

Figure 36.3: Schematic of the AM simulator at Sector 32 of the APS. Synchrotron X-ray radiography and diffraction can be obtained during laser melting and solidification of bulk and/or powder samples [36.9].

Table 36.1: Experimental Conditions Evaluated

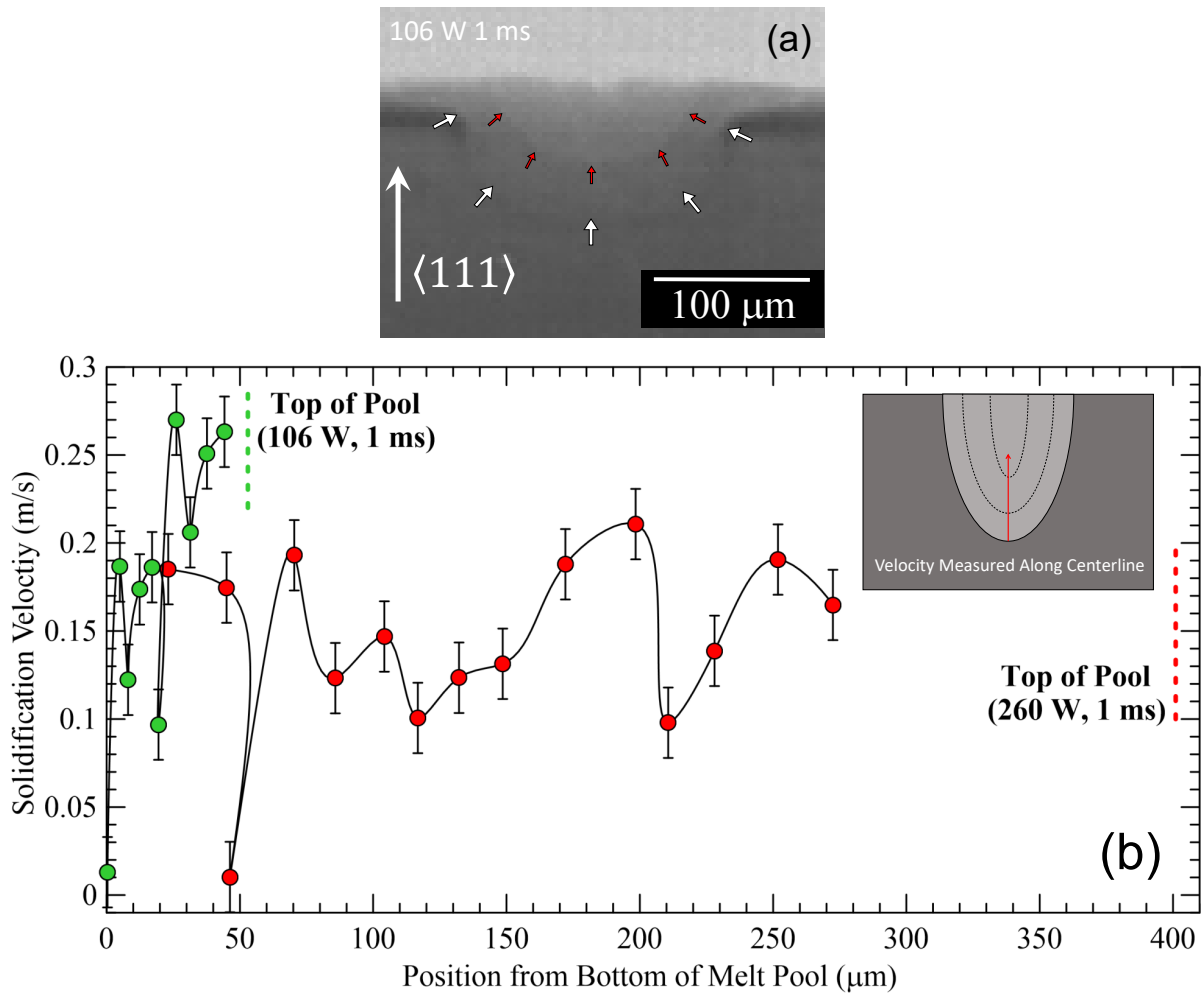| Sample Designation	R4-100	R4-110	R2-110	R2-111
Composition (wt %)	Ni-22.2Mo-2.8Al		Ni-1.9Mo-6.6Al	
Orientation of Build Direction	$\langle 100 \rangle$	$\langle 110 \rangle$	$\langle 110 \rangle$	$\langle 111 \rangle$
Orientation of Normal Direction	$\langle 100 \rangle$	$\langle 100 \rangle$	$\langle 110 \rangle$	$\langle 110 \rangle$
Laser Spot Melting Parameters	106, 156, 208, or 260 W for 1 ms			

36.5

Figure 36.4: (a) Example radiograph of R2-111 laser melted at 106 W for 1 ms. White arrows indicate the position of the solid-liquid interface at the beginning of solidification. Red arrows point to the position of the solid-liquid interface at a later time. (b) Measurements of the velocity of the solid liquid interface (solidification velocity) as a function of position from the bottom of the melt pool made from radiography images. Solidification velocity is observed to increase from the bottom to the top of the melt pool. Higher solidification velocities are observed at the lower laser power condition (106 W) compared to the higher laser power condition (260 W).
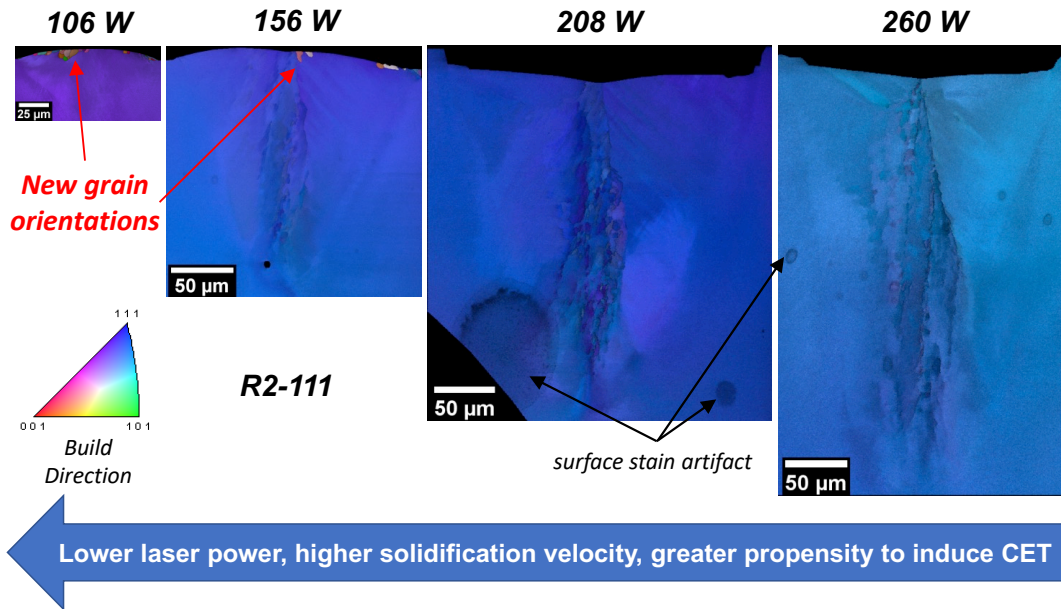
Figure 36.5: EBSD IPF + IQ maps of R2-111 samples laser melted with 106, 156, 208, and 260 W for 1 ms. The coloring of the IPF maps indicate the crystallographic orientation parallel to the build direction. The two lower power conditions (106 and 156 W) show new grain orientations at the tops of the melt pools. The presence of new grain orientations correlates with higher solidification velocities, which is expected to increase the propensity to induce the CET. The 208 and 260 W samples exhibit surface stain artifacts in the IQ maps. EBSD scans for these samples will be repeated following cleaning to remove the stains.
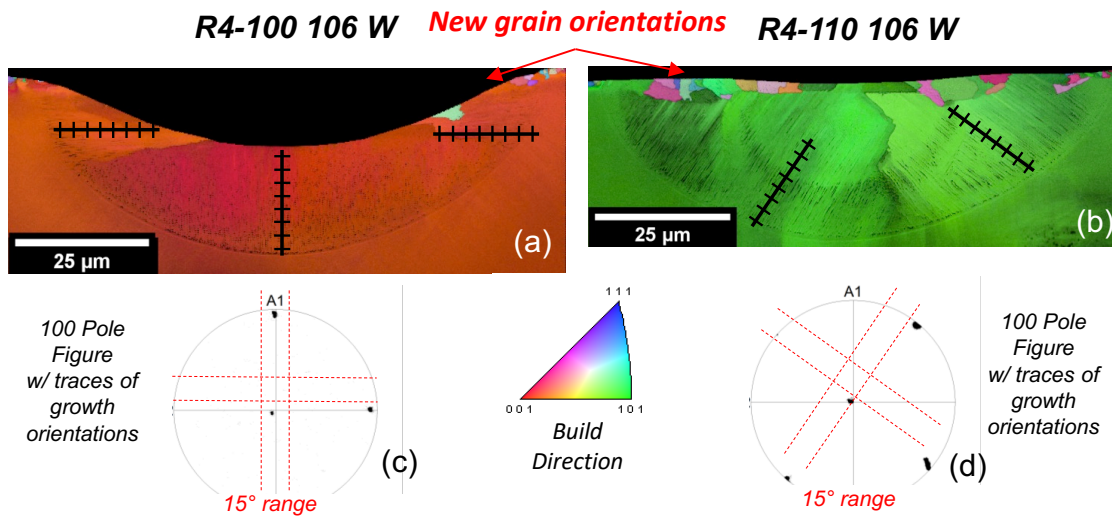

Figure 36.6: EBSD IPF + IQ maps of (a) R4-100 and (b) R4-110 samples laser melted with 106 W for 1 ms. The coloring of the IPF maps indicate the crystallographic orientation parallel to the build direction. The orientations of the elongated solidification microstructures are indicated in (a) and (b). Both substrate orientation exhibit new grain orientations at the top of the weld pools indicating the CET has be induced. (c) and (d) show ⟨100⟩ pole figures with traces of the orientations of the solidification growth orientations. Within a range of 15°, the traces of the growth orientations contain ⟨100⟩ directions indicating the likelihood of crystallographic dendritic solidification. All conditions evaluated suggest similar crystallographic dendritic solidification.

36.7

R2-110 106 W   **R4-110 106 W**

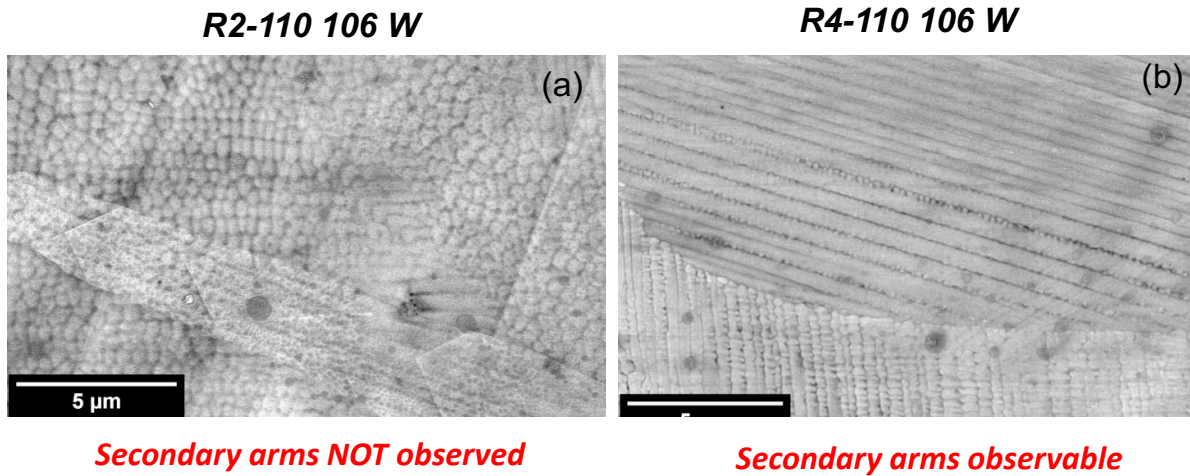*Secondary arms NOT observed*   *Secondary arms observable*

Figure 36.7: SEM BSE micrographs of the top of spot melt pools of (a) R2-110 and (b) R4-110 melted with a laser power of 106 W for 1 ms. Secondary dendrite arms are not observed in the lower Mo content (1.9 wt %) alloy R2, whereas secondary dendrite arms are observed in the higher Mo content (22.2 wt %) alloy.